Research Article

Method of Entry Layout under Synergistic Effects of Abutment Stress and Dynamic Stress

Wenlong Shen [ID],[1,2,3] Guocang Shi,[1] Meng Wang,[1] Tenglong Rong [ID],[1,3] Yungang Wang [ID],[1,3] Ruifeng Zhang,[1] Xiangyu Wang,[2] and Jianbiao Bai[2]

[1]*Henan Key Laboratory for Green and Efficient Mining & Comprehensive Utilization of Mineral Resources, School of Energy Science and Engineering, Henan Polytechnic University, Jiaozuo, Henan 454000, China*
[2]*State Key Laboratory of Coal Resources and Safe Mining, Key Laboratory of Deep Coal Resource Mining Ministry of Education, China University of Mining & Technology, Xuzhou, Jiangsu 221116, China*
[3]*State Collaborative Innovation Center of Coal Work Safety and Clean-Efficiency Utilization, Jiaozuo, Henan 454000, China*

Correspondence should be addressed to Tenglong Rong; rongtenglong@126.com and Yungang Wang; cumtwyg@163.com

In underground mining engineering, rocks around the entry are always subjected to large plastic deformation disasters, such as supporting body failure, roof rock collapse, and even rock burst under abutment stress and dynamic stress. To improve the stability of these rocks, the entry layout under abutment stress and dynamic stress (ELAD) method was put forward to protect the entry from high abutment stress and dynamic stress. Dynamic disturbance intensity (DDI) was determined as the key evaluation index in ELAD, which was divided into "Slightly Disturbed Type," "Moderately Disturbed Type," and "Violent Impact Type" by the dynamic disturbance threshold (DDT) and dynamic large-deformation threshold (DLT). The established servo calculation algorithm was applied into a dynamic and static numerical analysis model with FLAC^{3D500} software for the solving of DDT and DLT by the method of zero growth DDI of plastic failure zone and the engineering-permitted limitation deformation. This model was validated by comparing the displacement of entry with the measured results in the field. The model results validated that the entry should keep away from the dynamic stress of Violent Impact Type firstly and then be arranged in the zone where the dynamic stress belongs to Slightly Disturbed Type. DDT increases linearly and DLT decreases with a power function as the increasing of the abutment stress. ELAD method is reliable to protect this kind of underground entry and its applicability will be improved by the support resistance by comparing the results from ELAD with those from the widely used methods for field investigation discussion. The analysis procedure can be repeatable and necessary since the rock and coal materials may be different in geological and engineering conditions.

1. Introduction

Underground space has become one of the widely used resources during social development in recent years, and it will provide security for human civilization for a long time in the future [1–3]. Entry is one of the underground spaces which mainly provides auxiliary transportation and ventilation function in the underground longwall mining engineering as the tail entry shown in Figure 1. Its stability is always governed by the loading stress, the mechanical behavior, and the support resistance. Influenced by the dynamic disturbance and the abutment stress, the stress will

change into another state in the rock around the entry [4]. This entry will suffer from large deformation disasters, such as supporting body failure, roof rock collapse, and even rock burst when the disturbance and stress is large enough, which threatens the normal operation of mining engineering [5]. For a specific geological condition, reduction of the loading stress has been a popular way to protect this entry from large deformation disasters in longwall coal mining engineering [6].

The loading stress mainly consists of original stress, abutment stress, and dynamic stress [7–9]. The abutment stress is the loading effect of the overburden rocks' weight

(a)

(b)

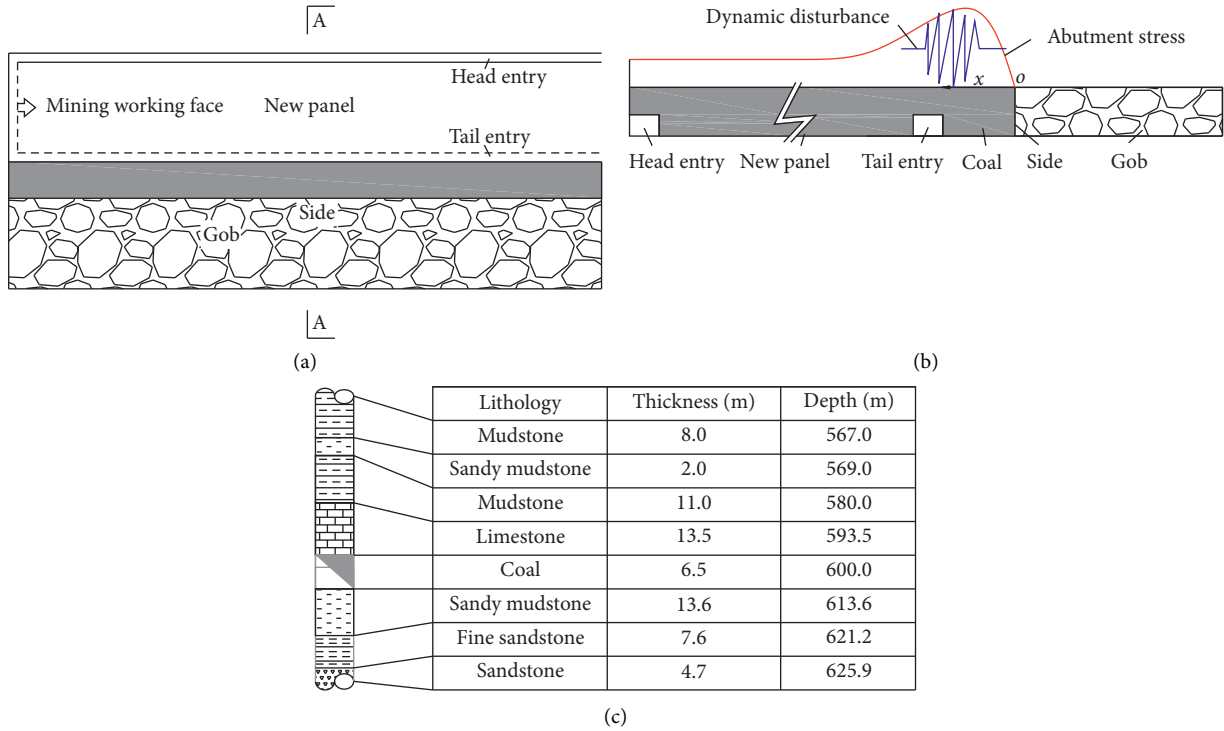| Lithology	Thickness (m)	Depth (m)
Mudstone	8.0	567.0
Sandy mudstone	2.0	569.0
Mudstone	11.0	580.0
Limestone	13.5	593.5
Coal	6.5	600.0
Sandy mudstone	13.6	613.6
Fine sandstone	7.6	621.2
Sandstone	4.7	625.9

(c)

FIGURE 1: Geological and engineering conditions of the entry. (a) Mining engineering plan; (b) A-A cross section in (a); (c) local drilling histogram. The gob has been in consolidation before the tail entry driving begins. The tail entry with dimensions of 5.0 m in width and 4.0 m in height is arranged along the coal floor and it is going to be excavated after its location is determined.

above the worked-out area on the rock around the worked-out area, which always results in the increasing of the stress in the rock [10]. The dynamic stress is the vibrational stress wave which comes from the rupture of rock, impact of caving rock, vibration of blasting, vibration of machines, and other physical motions, which always changes the strain rate of the rock [11]. The mechanical behavior of this rock has been divided into creep, static, weak dynamic, dynamic, and strong dynamic according to the strain rate [12]. The strength of the rock will increase surely with the increasing of the strain rate when the strain rate belongs to dynamic and strong dynamics. Differently, it keeps stabilization or increases slowly with the increasing of the strain rate when the strain rate belongs to static or weak dynamics. The entry will be subjected to tensile and shear fracture in brittle rock, and it will be yielded to large plastic deformation in soft rock during the coupled static-dynamic loading process [13–16]. The existing achievements, mainly concerning shallow-buried civil engineering [17–21] and underground metal mining engineering [22–26], provide precious guidance for analyzing the large deformation behavior of the entry in underground coal mining engineering [27–31]. Finding the mechanical behavior of rock around the entry under the synergistic effects of the abutment stress and dynamic stress is beneficial to the reduction of the large deformation.

Loading stress relief methods can be divided into four widely used types, including solid backfilling technology, cutting roof technology, depressurizing borehole technology, and the entry layout technology [32]. The solid backfilling technology is able to protect the roofs from movement intensively and avoid the generation of abutment stress and dynamic disturbance [33–35]. However, the expensive material consumption makes the solid backfilling technology apply limitedly in the mining area where there are surface buildings, water sources, and railways. Cutting roof technology is good at reducing the abutment stress by changing the bearing structure of the roof [36–41]. However, the influences of remolded structures on the movement of the upper roof structures were not considered, and the cutting roof technology is restricted by working space, technical defects, and costs. Depressurizing the borehole technology has the ability to transfer the abutment stress from the area with a borehole to the area without borehole [42–45]. However, this borehole changes the mechanical behavior of the rock, always making the rock in reduction of strength, and it is fairly difficult to determine a reasonable borehole parameter. Relatively, entry layout technology has advantages in avoiding of high stress, reduction of costs, and increasing of resource recovery, which is the most popular method in coal mining engineering [46–48]. The famous Wilson's equation [49] and ultimate balance theory [50, 51] can protect the entry from abutment stress but ignore the effects of dynamic disturbance. A new method needs to be found to design the location of the entry under the abutment stress and dynamic disturbance.

In this work, ELAD method was put forward to design the location of the entry. Evaluation index was determined and judging criteria were established for ELAD. After that, a numerical analysis model with servo calculation algorithm was established and validated to solve the evaluation index.

The result of ELAD method was compared with the results of several widely used methods. This comparison indicates that ELAD method has three advantages. In addition, a field investigation discussion also verified that ELAD method is reliable to design the location of the entry.

2. Method of ELAD

The amplitude of the stress wave was demonstrated as the significance influence factor of the entry deformation compared with the wave frequency and dynamic time [52]. The dynamic disturbance intensity (DDI) playing the index role in the method of ELAD was put forward to analyze the changes in stress, displacement, and plastic zone of the rocks around the entry under the influence of stress wave. For example, DDI of stress can be calculated by the ratio of the stress under the stress wave disturbance and the stress without the stress wave disturbance for any point of the rock. With the identical method, DDI of displacement, DDI of plastic failure zone, and DDI of crack can be obtained.

Plastic deformation plays the principal role in elastic-plastic deformation of the rock around the entry under the stress wave and abutment stress [53]. Dynamic disturbance threshold (DDT) was proposed to prevent the rock from additional plastic deformation (APD), which can be calculated by the method of zero growth DDI of plastic failure zone. This method has the advantage of limiting the expansion of the plastic zone of the rock around the entry under the stress wave, which makes DDI of the plastic failure zone equal one. DDT equals the amplitude of this stress wave.

Underground mining engineering was permitted in large deformation of entry compared with the shallow tunneling engineering [18], because of its short service life [53]. This underground entry is vulnerable to large deformation disasters (LDD) such as roof caving, rib caving, and rock burst when the deformation is large enough. Dynamic large-deformation threshold (DLT) was proposed to prevent the rock from LDD, which can be calculated by the method of engineering-permitted limitation deformation. This method has the advantage of making the deformation be in the limitation range for the entry under the stress wave which is permitted by the engineering. Additionally, DLT equals the amplitude of this stress wave.

DDT and DLT will change as the static stress varies from the original stress to the abutment stress. For a specific stress condition, DDI can be divided into "Slightly Disturbed Type," "Moderately Disturbed Type," and "Violent Impact Type" according to the values of DDT and DLT. Dynamic stress of Slightly Disturbed Type is determined as the dynamic stress less than DDT, that of Violent Impact Type is determined as the dynamic stress more than DLT, and that of Moderately Disturbed Type is determined as the dynamic stress between DDT and DLT.

The underground entries should keep away from the dynamic stress of Violent Impact Type firstly and then be arranged in the zone where the dynamic stress belongs to Slightly Disturbed Type. By symbol description, the entries should keep away from the zone of the results of $R(x) \geq L(x)$ firstly and then be arranged in the zone of the results of $R(x) \leq D(x)$, where $R(x)$ is the distribution of the potential stress wave, MPa; $D(x)$ is the distribution of DDT of the abutment stress function $f(x)$, MPa; $L(x)$ is the distribution of DLT of the abutment stress function $f(x)$, MPa; and x is the location away from the side of the gob, m. The detailed solution is presented as shown in Figure 2.

3. Numerical Simulation Model

3.1. Model Establishment

3.1.1. Constitutive Behavior of the Materials. Coal and rock materials are vulnerable to elastic and plastic deformation under the experimental loading test (Figure 3) with the displacement loading S_e (equation (1)). Mohr–Coulomb model is able to simulate the elastic deformation behavior approximatively for rock materials [54], but it is not suitable for simulating the strain softening behavior of the coal material. Taking the attenuation of the strength parameters, strain softening model has a good agreement with the plastic deformation of coal material (Figure 3(a)). The mechanical parameters of coal and rock materials are as shown in Table 1, and the attenuation rule of the cohesion parameter is as shown in Table 2. The displacement loading is S_σ as the description in equation (1).

$$\begin{cases} S_e = 2 \times 10^{-5} \text{m/second}, \\ S_\sigma = 2 \times 10^{-8} \text{m/step}. \end{cases} \tag{1}$$

The constitutive models are all accepted by the dynamic analysis in FLAC^{3D}, because the fully nonlinear analysis method based on the explicit finite difference scheme is used to solve the full equations of motion, using lumped grid point masses derived from the real density of surrounding zones in FLAC^{3D} [55]. Strain softening model is determined to simulate the dynamic response of the coal material and Mohr–Coulomb model is used to simulate the dynamic response of the rock materials. For the coal sample example, its dynamic strain behaviors are as shown in Figure 4.

The coal sample with the uniaxial compression stress 3.69 MPa (approximately 25 percent of the uniaxial compression strength) has enough capacity to bear the stress wave when the amplitude of the compression shear stress wave is less than 22.15 MPa. Within 22.15 MPa, the stress wave makes the coal sample vibrate elastically, and the vibration amplitude of the coal sample increases as the increase of the amplitude of compression shear stress wave. Both the stress and the strain can return to the original value due to the fact that the stress increases linearly first and then decreases linearly along the original path as the strain varies. However, the stress and vertical strain cannot return to the origin state when the amplitude of the stress wave is more than 22.15 MPa. The coal sample changes in deformation behavior from small elastic state to large plastic state.

At the same time, this coal sample, with the uniaxial compression stress 3.69 MPa (approximately 25 percent of the uniaxial compression strength), has enough capacity to
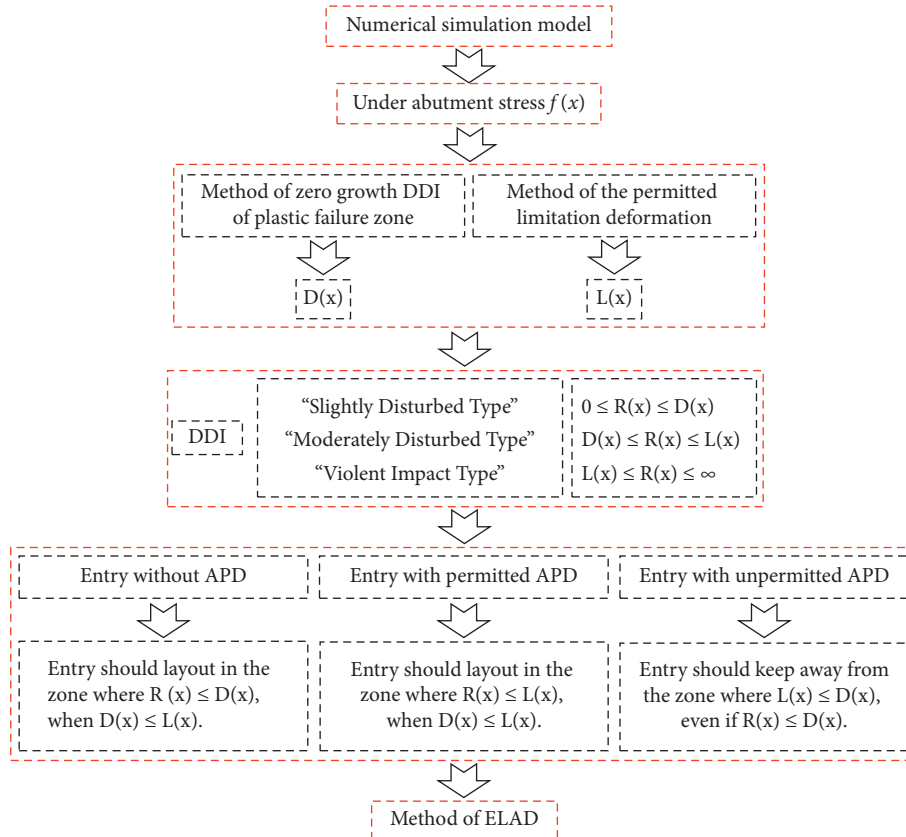
FIGURE 2: Detailed solution of the entry layout method.

bear the stress wave when the amplitude of the tensile stress wave is less than 9.78 MPa. Within 9.78 MPa, the stress wave makes the coal sample vibrate elastically and the vibration amplitude of the coal sample increases as the increase of the amplitude of tensile stress wave. Both the stress and the strain can return to the original value due to the fact that the stress increases linearly first and then decreases linearly along the original path as the strain varies. When the amplitude of the tensile stress wave reaches 7.38 MPa, the deformation behavior changes from compression to tensile state. However, the stress and strain cannot return to the origin state when the amplitude of the stress wave is more than 9.78 MPa. The coal sample changes in deformation behavior from small elastic state to large plastic state.

The limitation of the compression-shear stress wave amplitude decreases linearly and the limitation of the tensile stress wave increases linearly as the increase of the static stress loaded in the submodel, which are the damaged mechanism of the coal material. The average strain rate is $4.5 \, s^{-1}$ between $0.1 \, s^{-1}$ and $10 \, s^{-1}$ which belongs to the weak dynamics [12]. Therefore, the effect of the strain rate on the strength of the coal material is not considered in the numerical model.

3.1.2. Model of Static Calculation. A three-dimensional numerical model was established with the geometric dimension being $65 \times 65 \times 65$ m along x, y, and z axial directions in FLAC^{3D} software [55]. According to the uniform zone dimensions and the solution time in the numerical model [56], the mesh size along both x direction and y direction was determined as 1 m for every rock stratum. Those along z direction are determined as 0.94 m, 0.95 m, 0.97 m, 0.93 m, 0.96 m, 1.0 m, 1.0 m, and 1.0 m, respectively, for the eight rock strata from the bottom (sandstone) to the top (mudstone) (Figure 1(c)). The left, right, front, back, and bottom sides of the model were fixed in displacement along the normal direction. The top side of the model was loaded with a uniform vertical stress for simulating the abutment stress. After the abutment stress was initialized in the model, the entry with a dimension 5×4 m was developed in the center of the numerical model. Calculation of the numerical model was carried out to simulate the deformation behavior of the entry under abutment stress until the maximum unbalance force was less than 10^{-5} N. The in situ vertical stress, maximum horizontal principal stress, and the minimum horizontal principal stress are 15.0 MPa, 14.73 MPa, and 8.53 MPa [57]. The maximum principal horizontal stress has an orientation of N43.7°W which has an angle 46.3° with the direction of the entry driving. The horizontal principle stress resolution must be carried out to establish a geological stress as the field condition in the numerical simulation model [58]. The input maximum horizontal principle stress was calculated as 16.54 MPa perpendicular to the axial direction of the entry driving and the input minimum horizontal principle stress was calculated as 16.34 MPa towards to the axial direction of the entry driving.
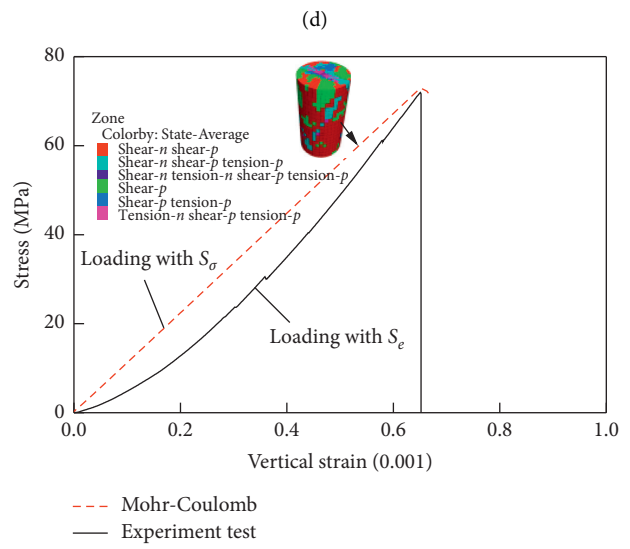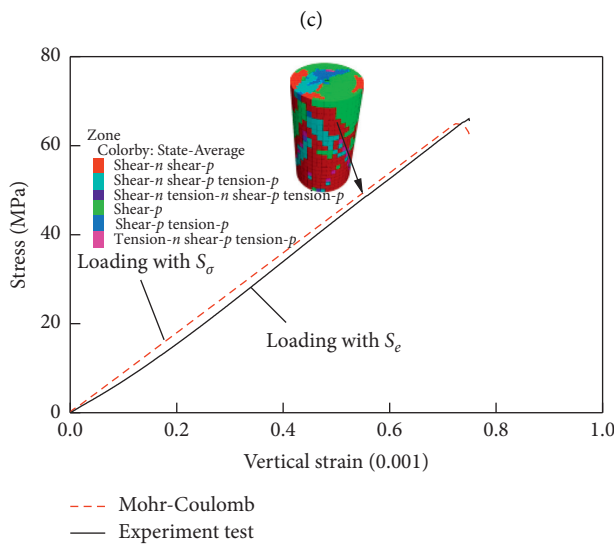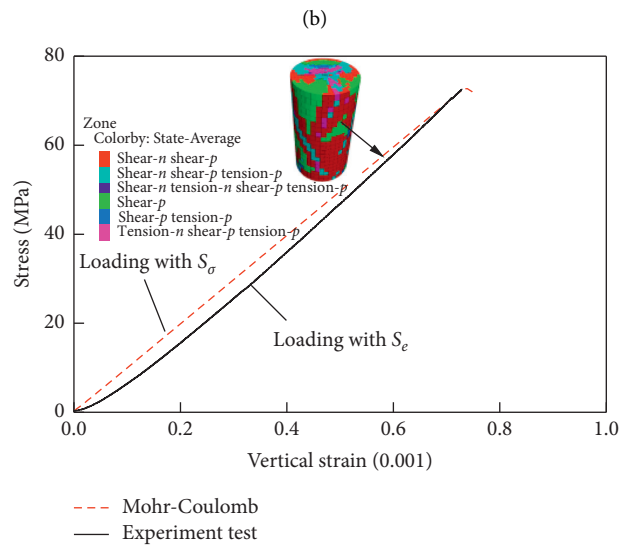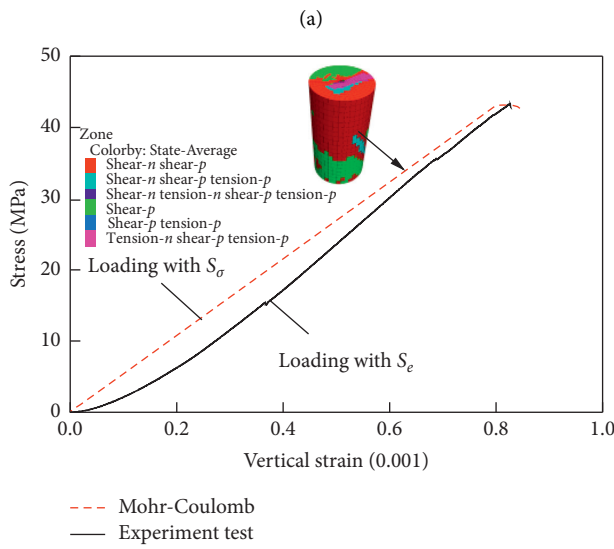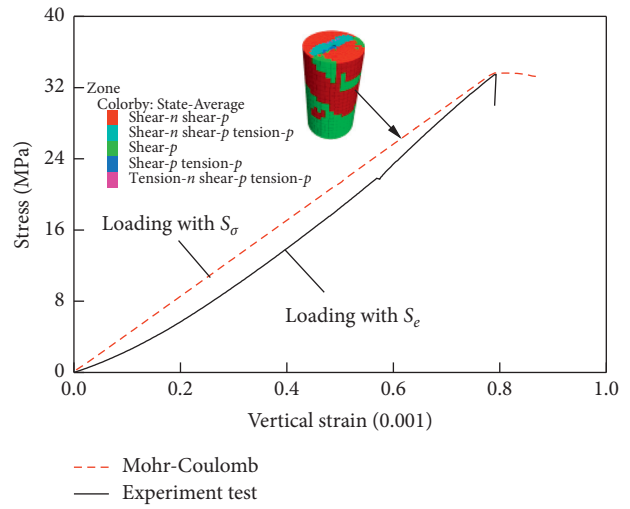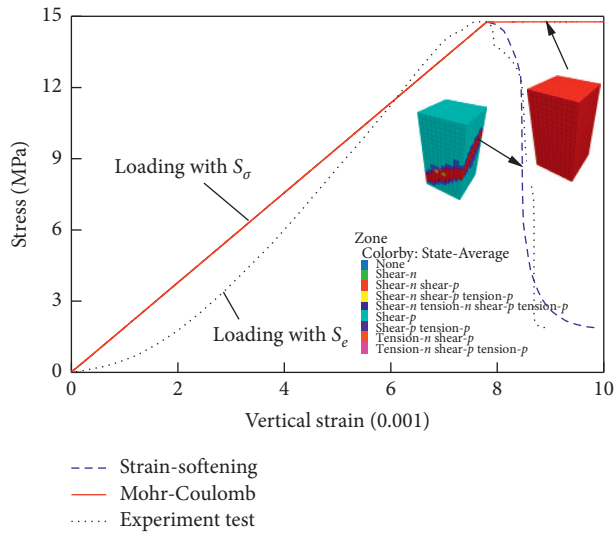
FIGURE 3: Relationship between stress and strain under uniaxial compression test. (a) Sample of coal. (b) Sample of mudstone. (c) Sample of sandy mudstone. (d) Sample of sandstone. (e) Sample of limestone. (f) Sample of fine sandstone.

TABLE 1: Parameters of model material.

Lithology	Density (kg/m³)	Bulk modulus (GPa)	Shear modulus (GPa)	Internal friction angle (°)	Cohesion (MPa)	Tensile strength (MPa)
Mudstone	2400	2.05	1.86	52	5.80	1.60
Sandy mudstone	2580	2.85	2.28	57	6.40	1.90
Mudstone	2400	2.05	1.86	52	5.80	1.60
Limestone	2640	4.62	3.83	65	7.20	2.20
Coal	1400	1.00	0.80	38	3.60	1.20
Sandy mudstone	2580	2.85	2.28	57	6.40	1.90
Fine sandstone	2600	5.85	4.76	67	7.40	2.40
Sandstone	2620	4.96	4.27	65	7.20	2.30

TABLE 2: Attenuation rules of the cohesion parameter for the coal material.

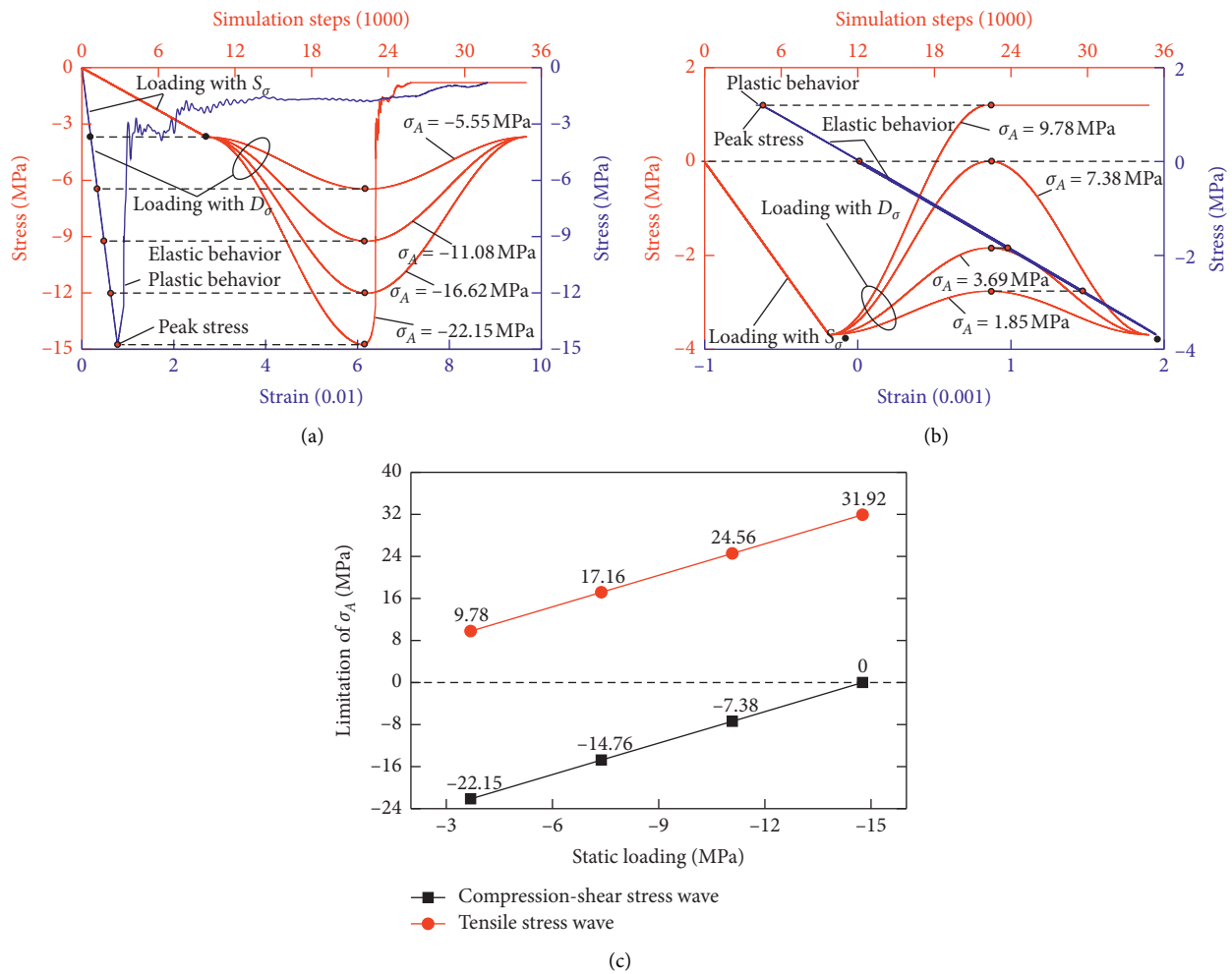| Plastic strain	0.00	0.01	0.01	. . .	1.00
Cohesion, MPa	3.60	2.76	0.14	. . .	0.14

FIGURE 4: Relationship between stress and strain under Dσ. (a) Dσ plays the compression-shear role in the submodel; (b) Dσ plays the tensile role in the submodel; (c) limitation dynamic stress of the submodel under different static loadings; the curves with red line describe the relationship between stress and simulation steps in Figures 4(a) and 4(b); the curves with blue line describe the relationship between stress and strain.

3.1.3. Model of Dynamic Calculation.

The length of every zone edge 1 m is less than tenth of the wavelength, which agrees with the calculation requirement for the numerical model. Static viscous boundary conditions were used to improve the calculation efficiency and reduce the reflection effects of the dynamic calculation process of the numerical model. Rayleigh damping was used to simulate the friction behavior between the coal materials. By numerical simulation, the minimum critical damping ratio was determined as 0.005 and the minimum center frequency was determined as the natural vibration frequency of the model 3.8 Hz. The dynamic time was determined as 0.4 seconds to supply enough time for the balance of every zone in the model. The cosine shear stress wave was applied to the surface of the model to simulate the dynamic stress as shown in equation (2). The effective time of the dynamic stress was determined as 0.02 seconds

$$D_\sigma = 0.5\left(1 - \cos\left(2\pi f t\right)\right) * \sigma_A, \tag{2}$$

where D_σ is the shear stress wave, MPa; f is the vibration frequency, Hz; t is the time of the dynamic calculation, s; and σ_A is the amplitude of the shear stress wave, MPa.

3.1.4. Verification of Numerical Model.

The displacement was determined as the analysis index to validate the numerical model consisting of the Mohr–Coulomb model for the rock material and the Strain-Softening model for the coal material during the entry development. Measuring of displacement with a steel ruler has been carried out during the development of the head entry in the field. The displacement increases quickly and then reaches a relatively stable value as shown in Figure 5. The simulated results using the numerical model show great agreement with the measured results in the field, which indicates that this numerical model can be used to analyze the displacement of the entry under this kind of geological conditions.

3.2. Simulation Plans.

First, five simulation cases were determined to investigate the dynamic response of the entry under the condition of the peak stress of the abutment stress (35 MPa), the original vertical stress (15 MPa), and their midvalue (25 MPa) in the field as shown in Table 3. The dynamic stress σ_A was determined to analyze DDI, varying between 0 MPa and 20 MPa. Second, the evolutions of DDT and DLT were solved as the static stress varied from 15 MPa to 35 MPa according to the dynamic threshold algorithm as shown in Figure 6. Third, DDI was divided into three strength grades including "Slightly Disturbed Type," "Moderately Disturbed Type," and "Violent Impact Type," according to the values of DDT and DLT. Finally, $L(x)$ and $D(x)$ were determined to layout the entry under the condition of the abutment stress $f(x)$ and the potential dynamic stress $R(x)$.

3.3. Results

3.3.1. Evolution of DDI.

DDI presents an increasing trend as the increasing of the stress wave amplitude. For example,
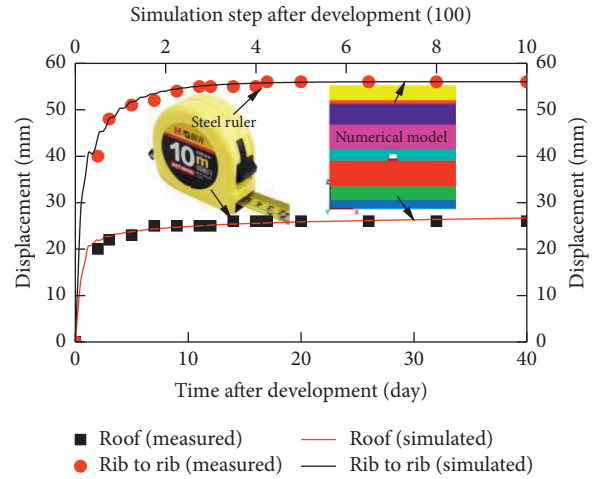

FIGURE 5: Comparison between the measured and simulated displacement.

TABLE 3: Simulation plans.

Abutment stress (MPa)	Dynamic stress, σ_A (MPa)				
15	0	5	10	15	20
25	0	2	4	6	8
35	0	2	4	6	8

DDI of plastic failure zone and that of displacement increase with an increasing gradient as the increasing of the stress wave amplitude (Figure 7). This kind of failure and deformation behavior will be in a state of slowdown as the input static stress increases. For example, both increasing amplitudes of DDI of plastic failure zone and DDI of displacement decrease as the increasing of the static stress. And, this kind of reduction amplitude of DDI will increase as the increasing of stress wave amplitude. However, the deformation of entry under the stress wave is larger than that without the influence of stress wave no matter how much the stress wave amplitude is.

3.3.2. Grades of DDI.

DDT presents a linear increasing trend and DLT presents a reduction trend as the increasing of the abutment stress when the engineering-permitted limitation deformation is determined as 200 mm with a security coefficient of 1.5 as shown in Figure 8. DLT is larger than DDT for this entry when the entry was loaded by the abutment stress between 15 MPa and 20 MPa. Using DDT and DLT, DDI was divided into three grades including "Slightly Disturbed Type," "Moderately Disturbed Type," and "Violent Impact Type." With the reduction of the range of Moderately Disturbed Type, the ranges of Slightly Disturbed Type and Violent Impact Type increase as the abutment stress increases. In addition, DDT is larger than DLT when the entry is loaded by the abutment stress between 20 MPa and 35 MPa. The deformation of the entry is larger than the engineering-permitted limitation deformation under this kind of abutment stress no matter whether DDI belongs to "Slightly Disturbed Type" or not. This kind of entry is located
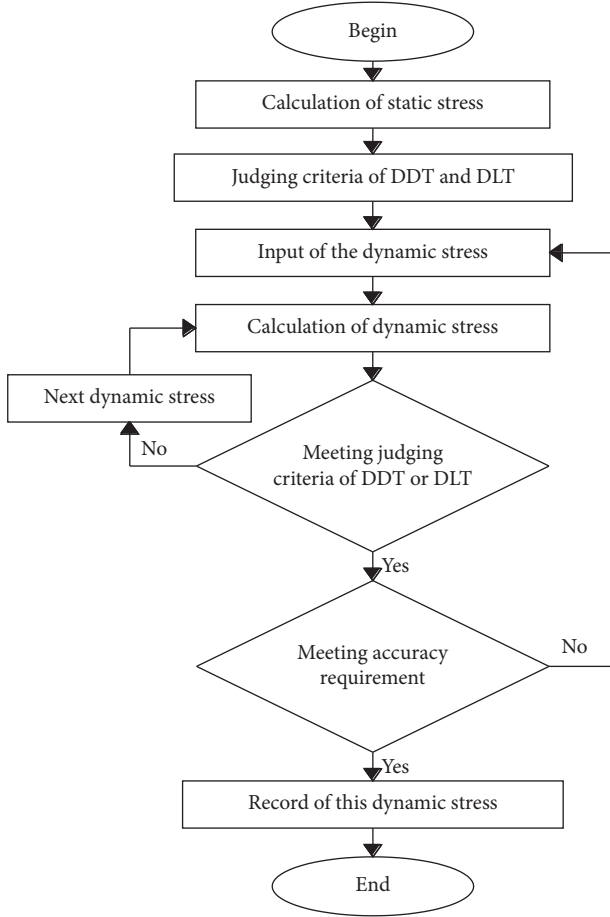
FIGURE 6: Dynamic threshold algorithm. The main process includes four sections. In the first section, the calculation of static stress is carried out using the numerical simulation model until the stress keeps balance. In the second section, the judging criteria of DDT and DLT are determined using the method of zero growth DDI of plastic failure zone and the engineering-permitted limitation displacement method. In the third section, the calculation of servo stress wave is carried out using the numerical simulation model until the stress wave meets the judging criteria and the accuracy requirement. Finally, DDT and DLT are recorded.

at the area where there exists high abutment stress. Some measures like rock support, rock consolidation, and entry layout must be taken to reduce the deformation of the entry under this kind of conditions.

3.3.3. Layout of Entry. The entry should layout at less than 4.91 m or more than 20.26 m away from the side of the gob according to the method of ELAD as shown in Figure 9. The piecewise function has been proved to be a reliable function to describe the distribution of the abutment stress $f(x)$ as shown in equation (3) [59]. By the data fitting process in MATLAB 2012b, the power function was determined to describe $D(x)$ and $L(x)$ as shown in Figures 10 and 11 and equations (4) and (5). The potential dynamic stress $R(x)$ comes from the liberating energy of 2.35×10^5 J during the mining-induced fracture of the interactional hard roof structures [9, 60]. The effect of this liberating energy on the

surrounding rock was replaced with a loading process of the equivalent dynamic stress, and this equivalent dynamic stress was determined as 9 MPa by using the method of elastic deformation energy [61]. The equivalent dynamic stress will propagate in the way of vibrating stress wave in sedimentary strata and its strength is in the state of attenuation when it passes through the discontinuous interface [62]. $R(x)$ was determined as shown in Figure 12 by the displacement discontinuity method [62] and it can be described by an exponential function as shown in equation (5). Model parameters are shown in Table 4.

$$f(x) = \begin{cases} a_1 x + a_2, & 0 \leq x \leq p, \\ a_3 e^{a_4 (x-p)} + a_5, & p \leq x \leq r, \\ \gamma H, & r \leq x \leq \infty, \end{cases} \quad (3)$$

where $f(x)$ is the abutment stress, MPa; a_1, a_2, a_3, a_4, and a_5 are parameters of the piecewise function, which can be determined by measuring data fitting; x is the distance to the side of the gob, m; p is the distance between the side of the gob and the location of the maximum value of the abutment stress, m; r is the distance between the side of the gob and the location of the original vertical stress, m; γ is the average volume weight of the geological strata, which can be calculated by the ratio of the cumulative sum of every stratum's volume weight and thickness and the cumulative thickness of geological strata, kN/m³; and H is the cumulative thickness of the geological strata, m.

$$D(x) = b_1 f(x)^{b_2} + b_3, \quad (4)$$

where b_1, b_2, and b_3 are parameters of the power function of $D(x)$, which can be determined by measuring data fitting.

$$L(x) = \begin{cases} c_1 f(x)^2 + c_2 f(x) + c_3, & x \leq c_4, \\ 0, & x \geq c_4, \end{cases} \quad (5)$$

where c_1, c_2, c_3, and c_4 are parameters of the power function of $D(x)$ and $L(x)$, which can be determined by measuring data fitting.

$$R(x) = d_1 e^{d_2 x} + d_3 e^{d_4 x}, \quad (6)$$

where d_1, d_2, d_3, and d_4 are parameters of the power function of $D(x)$ and $L(x)$, which can be determined by measuring data fitting.

4. Discussion

4.1. Characteristic of DDI. Plastic deformation behavior plays the main role in the reduction of the underground entry space, and the LDD will generate if the plastic deformation is large enough. The plastic deformation is mainly governed by the stress condition, the support resistance, and the material properties. For a determined geological condition, the plastic failure zone of the entry under high static stress is larger than that of the entry under low static stress, and converting the elastic zone into plastic zone needs larger dynamic stress, which are the reason for the increasing of DDT with the increasing of the static stress. Meanwhile, the
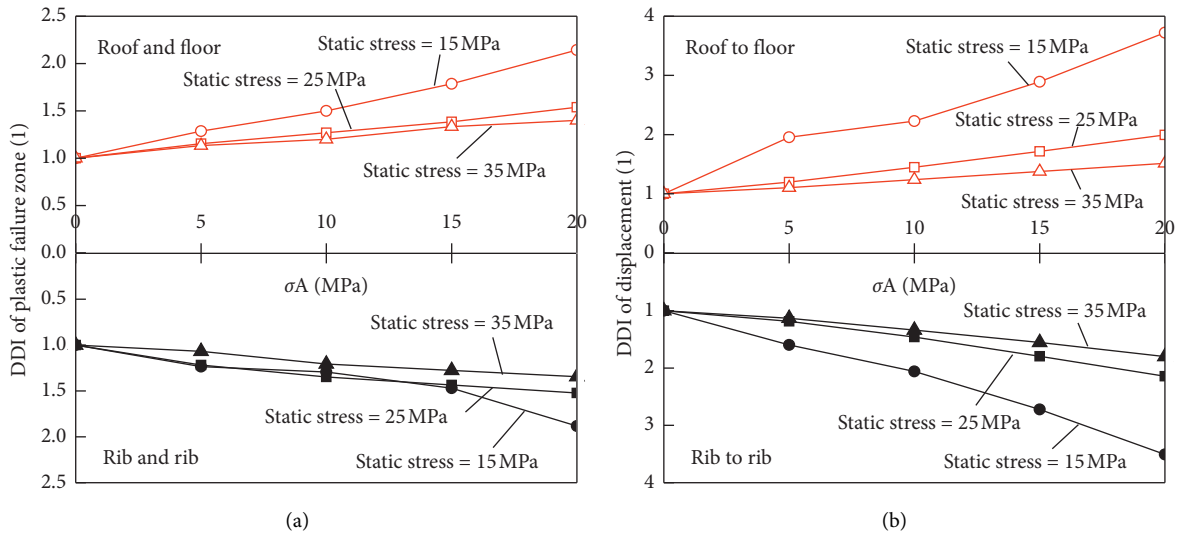
(a)

(b)

FIGURE 7: Evolution of DDI for the surrounding rock under different loadings. (a) DDI of plastic failure zone; (b) DDI of displacement.

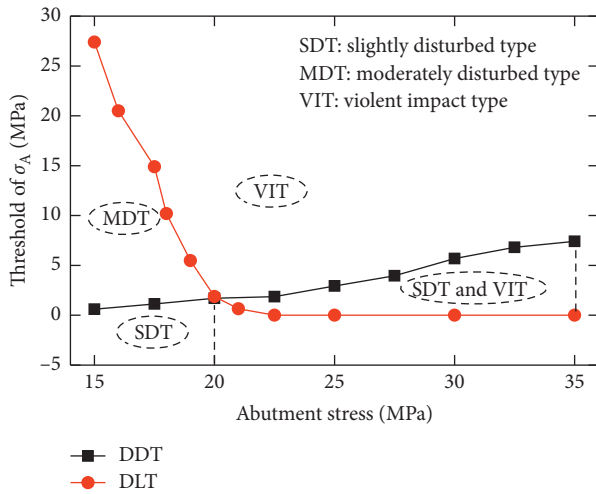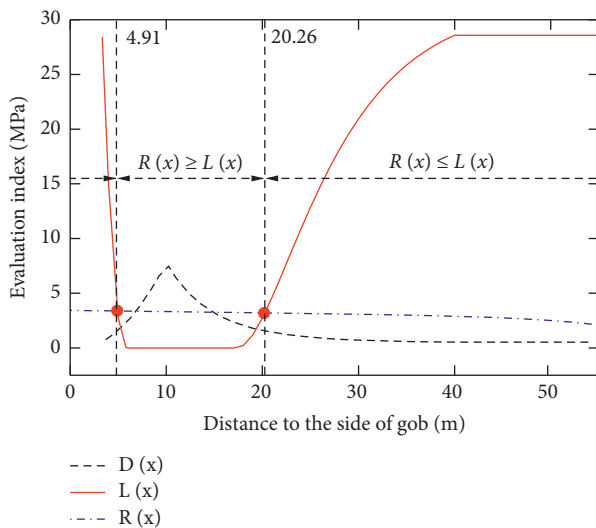FIGURE 8: Results of the disturbing dynamic threshold and the large deformation caused dynamic threshold.

$$D(x) = b_1 f(x)^{b_2} + b_3$$
$$R^2 = 0.98$$

- Numerical simulation data
- Fitting with power function

FIGURE 10: Relationship between DDT and abutment stress.

- D(x)
- L(x)
- R(x)

FIGURE 9: Distribution of evaluation index.

$$L(x) = c_1 f(x)^2 + c_2 f(x) + c_3$$
$$R^2 = 0.99$$

c_4 $L(x) = 0$

- Numerical simulation data
- Fitting with power function
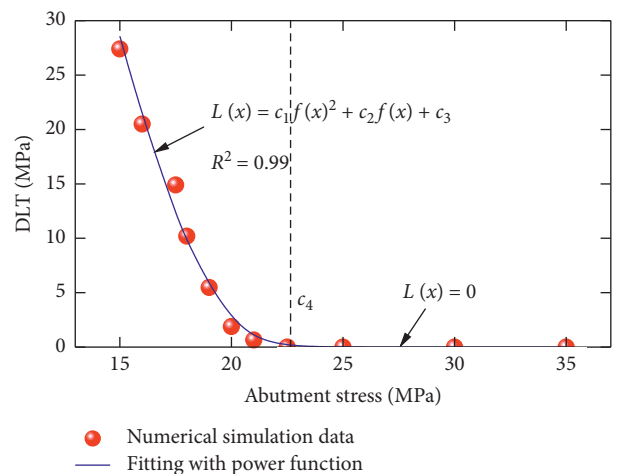
FIGURE 11: Relationship between DLT and abutment stress.

$$R(x) = d_1 e^{d_2 x} + d_3 e^{d_4 x}$$

$$R^2 = 0.99$$

- ● Displacement discontinuity method
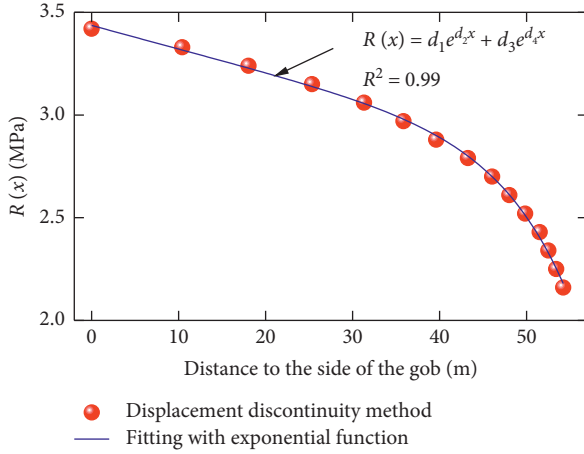- — Fitting with exponential function

Figure 12: Potential dynamic stress $R(x)$.

Table 4: Parameters used in the mathematical models.

Parameters	Values
a_1	2
a_2	15
a_3	20.37386
a_4	−0.13327
a_5	14.62614
b_1	0.001379
b_2	2.449
b_3	−0.5203
P	10
R	40
c_1	0.5463
c_2	−24.289
c_3	270
c_4	22.4
γH	15
d_1	−0.00075
d_2	0.1257
d_3	3.437
d_4	−0.00335

deformation of the entry under high static stress is larger than that of the entry under low static stress, which is the reason for the decreasing of DLT with the increasing of the static stress. DDI was divided into "Slightly Disturbed Type," "Moderately Disturbed Type," and "Violent Impact Type" by the distribution of DDT and DLT. DDI of plastic failure zone equals 1 and DDI of deformation is small when the entry is loaded by dynamic stress of the Slightly Disturbed Type. DDI of plastic failure zone is more than 1, and DDI of deformation increases clearly when the entry is loaded by the dynamic stress of Moderately Disturbed Type. DDI of plastic failure zone increases surely to more than 1 and DDI of deformation is large enough when the entry is loaded by the dynamic stress of Violent Impact Type.

4.2. Significance of ELAD. ELAD has three advantages in mechanical behavior, loading conditions, and deformation evaluation indexes for coal materials compared with the widely used Wilson's equation [49], ultimate balance theory [50, 51], and the existing numerical simulation method [63]. Firstly, postpeak strain softening behavior in Strain-Softening model is able to determine reliable values of the deformation evaluation indexes compared with the postpeak strain stabilization behavior in Mohr–Coulomb model for coal materials, which is considered by ELAD. Secondly, the underground entries sometimes suffer from the abutment stress and dynamic stress at the same time. The values of the deformation evaluation indexes are full of errors if the method considers the abutment stress or the dynamic stress separately. Finally, quantitative deformation evaluation indexes are beneficial to the entry layout compared with the qualitative deformation changes. For example, underground entries will face different engineering-permitted conditions, such as the entry without APD, the entry with permitted APD, and the entry with unpermitted APD. ELAD can be used to layout these underground entries by the method of zero growth DDI of plastic failure zone and the method of engineering-permitted limitation deformation. However, Strain-Softening model just describes the deformation behavior of the coal materials, which ignores the influences of the cracks and their internal fillings. This challenging problem will be considered in the next works in the future.

ELAD is compared with other widely used methods to design the underground entry layout under the same geological engineering condition in Table 5. The confined core is helpful for the stabilization of the coal pillar when the entry locates at more than 6.88 m away from the side of the gob, but the deformation of the entry will exceed the engineering-permitted value and the dynamic stress disturbance is ignored. The elastic core is large enough to protect the entry from large deformation disaster when the entry locates at more than 32.32 m away from the side of the gob; however, the 32.32 m wide coal pillar generates the reduction of the coal resource recovery. The stress is less than or equals the original stress when the entry locates at less than 3.34 m or more than 40.00 m away from the side of the gob, which is beneficial to the stabilization of the entry, but 40.00 m wide coal pillar is against the improvement of the coal resource recovery. The deformation is within the engineering-permitted deformation of 200 mm when the entry locates at less than 5.84 m or more than 17.13 m away from the side of the gob, which is applicable in the zone without the disturbance of the dynamic stress. In addition, the deformation is less than the engineering-permitted deformation of 200 mm without the disturbance of the dynamic stress when the Strain-Softening model is replaced with the Mohr–Coulomb model, which is inconsistent with the deformation behavior.

4.3. Effects of the Support Resistance. For the field case, the underground entries are always protected by the support technologies from LDD. Figure 13 presents the effects of the support resistance on the DDT and DLT. DDT and DLT increase with the increasing of support resistance, which means this entry is able to bear larger dynamic stress with the help of the support resistance. DDT is larger than DLT, because the elastic-plastic deformation of the entry reaches the engineering-permitted value before the generation of

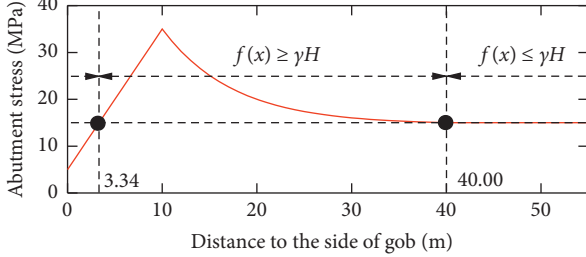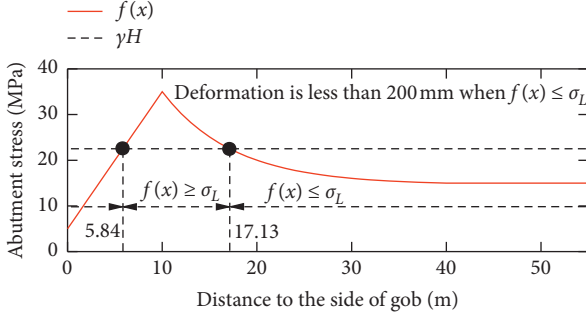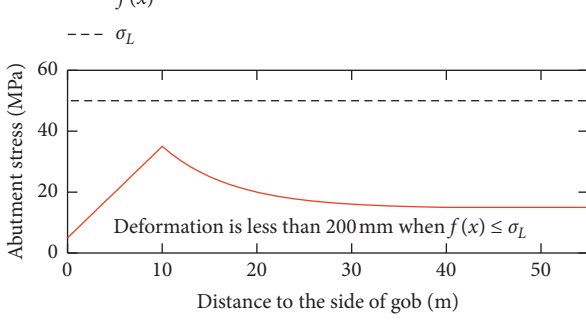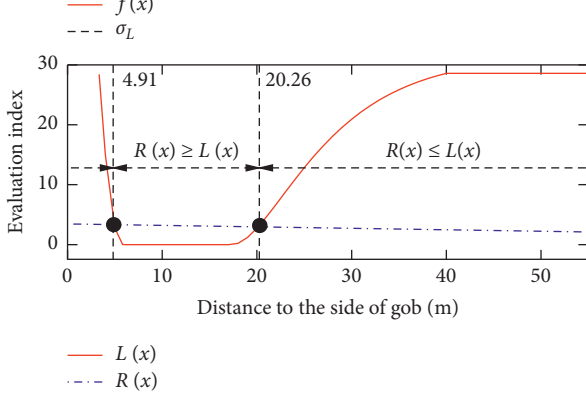TABLE 5: Underground entry layout comparison.
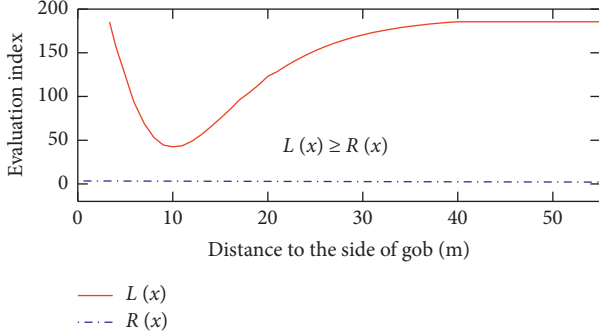
Methods	Evaluation indexes	Solving process	Results
(1) Confined core concept with Wilson's equation [49]	$r_0 = 2m/\sqrt{1 + \sin\varphi_0/1 - \sin\varphi_0} \, (\tan(1 + \sin\varphi_0/1 - \sin\varphi_0) - 1)\ln(K\gamma H/\sigma_0)$	$x \geq 2r_0$	$x \geq 6.88$ m
(2) Elastic core concept with ultimate balance theory [50]	$r_0 = mA/\tan\varphi_0 \ln[(K\gamma H + C_0/\tan\varphi_0)/(C_0/\tan\varphi_0 + P_x/A)]$	$x \geq 2r_0 + 2m$	$x \geq 32.32$ m
(3) Stress relief method with stress less than original stress [63]		$f(x) \leq \gamma H$	$x \leq 3.34$ m or $x \geq 40.00$ m
(4) Engineering-permitted deformation method with Strain-Softening model and without dynamic stress [47]		$f(x) \leq \sigma_L$	$x \leq 5.84$ m or $x \geq 17.13$ m
(5) Engineering-permitted deformation method with Mohr–Coulomb model and without dynamic stress [53]		$f(x) \leq \sigma_L$	$x \geq 0$ m
(6) ELAD method with Strain-Softening model		$R(x) \leq L(x)$	$x \leq 4.91$ m or $x \geq 20.26$ m

TABLE 5: Continued.

Methods	Evaluation indexes	Solving process	Results
(7) ELAD method with Mohr–Coulomb model		$R(x) \leq L(x)$	$x \geq 0\,\text{m}$

where r_0 is the width of the yield zone; m is the height of the mining space, 6.5 m; K is peak stress concentration factor, 2.33; σ_0 is the unconfined compressive strength, 14.76 MPa; A is lateral pressure coefficient, 1; P_x is the support strength on the face of the coal wall, 0.2 MPa; φ_0 is the internal friction angle of the coal material, 38°; C_0 is the cohesion of the coal material, 3.6 MPa; and σ_L is the permitted value of the abutment stress around the entry, MPa.
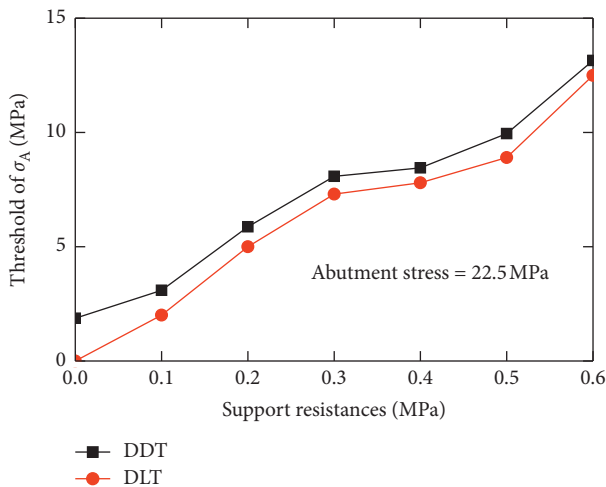

FIGURE 13: Effects of the support resistance on DDT and DLT.

APD under the abutment stress of 22.5 MPa. However, DLT can be larger than DDT when the value of the abutment stress changes to another value, such as the loading condition that the abutment stress varies from 15 MPa to 20 MPa (see Figure 8 for details).

The results of the entry layout by ELAD are different when the support resistance changes as shown in Figure 14. The acceptable location is determined as less than the maximal value or more than the minimal value away from the side of the gob and the unacceptable location is between them to layout the underground entry. The range of the acceptable location increases and the range of unacceptable location decreases with the increasing of the support resistance, which is helpful to protect the underground entry from the synergistic effects of abutment stress and dynamic stress. The entry layout can be determined by Figure 14 for a determined geological, engineering, and supporting condition.

4.4. Deformation Behavior for the Field Entry. To verify the reliability of ELAD method, field investigation works have been carried out in the subordinate San coal mine in Yangquan coal field. The maximum support resistance is calculated as 0.39 MPa. There were totally 10 anchor bolts and 8 anchor cables around the entry section. The anchor bolts are 880 mm in interval, 800 mm in row space, 20 mm in diameter, 2000 mm in length, and 150 kN in tensile fracture load in the entry roof. And, they are 1900 mm in interval, 800 mm in row space, 22 mm in diameter, 2000 mm in length, and 150 kN in tensile fracture load in the entry ribs. The anchor cables are 880 mm in interval, 800 mm in row space, 21.6 mm in diameter, 5200 mm in length, and 400 kN in tensile fracture load in the entry roof. And, they are 1900 mm in interval, 800 mm in row space, 21.6 mm in diameter, 5200 mm in length, and 400 kN in tensile fracture load in the entry ribs.

The entry was arranged tentatively at 10 m away from the side of the gob according to the successful case in the coal seam [64]. It suffered from large deformation in the roof during the entry driving. The roof convergence reached 265 mm, the floor convergence reached 565 mm, and the rib-to-rib convergence reached 413 mm. Anchor cables experienced body fracture failure in some areas, which threatened the stability of the entry roof. Mining engineers take some remedial measures to guarantee the system operation normally for this entry, which results in the waste of manpower and material resources. A single hydraulic prop, with an initial service load of 11 MPa, was applied to reinforce the support of the entry roof throughout the whole entry. Every failure anchor cable was replaced with a normal one. Driving heave rock in the floor was adopted several times. Representative field photos are as shown in Figure 15.

The maximum difference is the mechanical boundary condition of stress between the entry in San coal mine and the entry in Sijiazhuang coal mine. The geological and engineering condition shows several differences between the two coal mines, which can influence the distribution of the
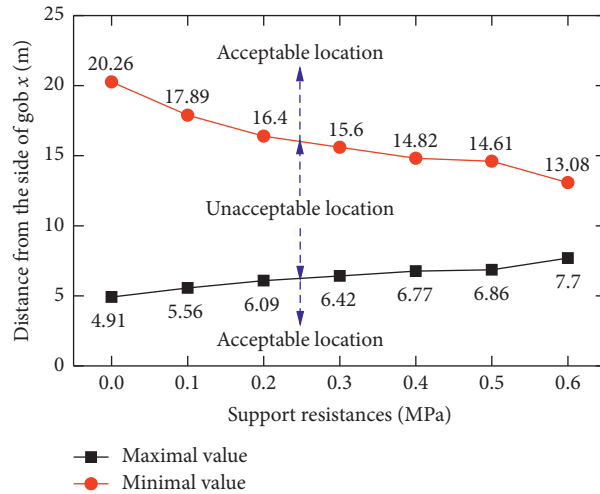
FIGURE 14: Effects of the support resistance on entry layout with ELAD.

(a)

(b)

FIGURE 15: Deformation characteristics of the entry in San coal mine in Yangquan coal field. (a) Anchor cable failure. (b) Rib deformation.

abutment stress [65]. For example, the average mining height, burial depth, and entry section width are 6.5 m, 600 m, and 5.0 m in San coal mine, and those are 5.5 m, 574 m, and 4.8 m in Sijiazhuang coal mine. The effect of the potential dynamic stress disturbance is not considered during determining the entry layout [6]. This result indicates that the entry can generate large deformation even though the successful case has similar geological and engineering condition and the analogy of experience has something unknown.

The entry should be arranged at less than 6.77 m or more than 14.82 m away from the side of the gob in San coal mine according to the results of ELAD method in Figure 14. ELAD method can protect the entry from the high static stress of abutment stress and dynamic stress of Violent Impact. Taking the resource recovery, San coal mine arranged the entry at 6 m away from the side of the gob. The deformation behavior is as shown in Figure 16, and the roof deformation is less than the engineering-permitted value of 200 mm, which verifies the reliability of ELAD method.
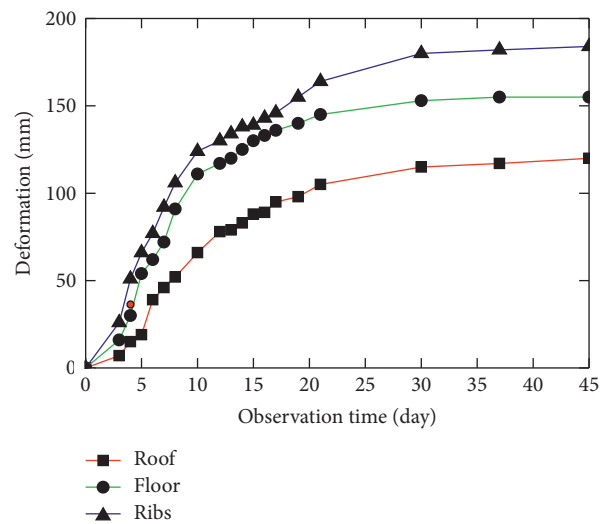

FIGURE 16: Deformation behavior of the entry.

5. Conclusions

It is hard to protect the underground entry from large deformation when the entry is loaded by the abutment stress and dynamic stress simultaneously in longwall mining engineering. The new method of ELAD was put forward to layout the entry. DDI is the key technology parameter in ELAD, which is divided into three grades, "Slightly Disturbed Type," "Moderately Disturbed Type," and "Violent Impact Type." The entry should keep away from the dynamic stress of Violent Impact Type firstly and then be arranged in the zone where the dynamic stress belongs to Slightly Disturbed Type. DDT and DLT were proposed to solve the grades of DDI, which can be calculated by the method of zero growth DDI of plastic failure zone and the engineering-permitted limitation deformation.

A dynamic and static numerical analysis model with FLAC^{3D500} software was established to solve DDT and DLT. To improve the reliability of this model, the Mohr–Coulomb model and Strain-Softening model for the rock and coal material deformation behavior were validated in detail with a uniaxial compression process. The Strain-Softening model and Mohr–Coulomb model are applied to simulate the deformation behavior of the coal and rock materials, respectively. The results of the model indicate that DDI increases linearly as the increasing of the dynamic stress. DDT increases linearly and DLT decreases with a power function as the increasing of the abutment stress. DDI equals 1 in the plastic failure zone and is small enough in deformation when the dynamic stress belongs to Slightly Disturbed Type. Those increase indeed when the dynamic stress belongs to Moderately Disturbed Type and they increase to large enough values when the dynamic stress belongs to Violent Impact Type.

ELAD method has advantages in mechanical behavior, loading conditions, and deformation evaluation indexes for coal materials compared with the widely used method, especially for the underground entry loaded with abutment stress and dynamic stress. The range of the acceptable location for entry layout increases indeed and the entry is able to bear larger dynamic stress with the increasing of support resistance, which improves the applicability of ELAD method. The field case discussion verified that ELAD method was reliable. The inadequacy of ELAD method is the influence of internal detailed discontinuous structures of the coal material, which will be considered in the next research project. The analysis procedure is repeatable and necessary since the coal material may differ in geological and engineering conditions.

Data Availability

All of the results are from the data of the curves.

Conflicts of Interest

The authors declare that they have no conflicts of interest.

Acknowledgments

References

[1] Q. Jiadong, D. Li, X. Li, and Q. Zhu, "Numerical investigation on the stress evolution and failure behavior for deep roadway under blasting disturbance," *Soil Dynamics and Earthquake Engineering*, vol. 137, Article ID 106278, 2020.

[2] R. Sterling and J. Zhao, "Editorial 2015 - celebrating 40 years of underground space and 30 years of tunnelling and underground space technology," *Tunnelling and Underground Space Technology*, vol. 50, p. A1, 2015.

[3] G. C. Zhang, Z. J. Wen, S. J. Liang et al., "Ground response of a gob-side entry in a longwall panel extracting 17 m-thick coal seam: a case study," *Rock Mechanics and Rock Engineering*, vol. 53, no. 2, pp. 497–516, 2019.

[4] M. Colwell, R. Frith, and C. Mark, "Analysis of longwall tailgate serviceability (ALTS): a chain pillar design methodology for Australian conditions," in *Proceedings of the Second International Workshop on Coal Pillar Mechanics and Design*, pp. 33–48, Vail, CO, USA, 1999.

[5] Z. Z. Zhang, M. Deng, J. B. Bai, X. Y. Yu, Q. H. Wu, and L. S. Jiang, "Strain energy evolution and conversion under triaxial unloading confining pressure tests due to gob-side entry retained," *International Journal of Rock Mechanics and Mining Sciences*, vol. 126, Article ID 104184, 2020.

[6] W.-L. Shen, J.-B. Bai, W.-F. Li, and X.-Y. Wang, "Prediction of relative displacement for entry roof with weak plane under the effect of mining abutment stress," *Tunnelling and Underground Space Technology*, vol. 71, pp. 309–317, 2018.

[7] G. C. Zhang, L. J. Chen, and Z. J. Wen, "Squeezing failure behavior of roof-coal masses in a gob-side entry driven under unstable overlying strata," *Energy Science & Engineering*, vol. 8, no. 7, pp. 2443–2456, 2020.

[8] J. F. Semblat, N. Lokmane, L. Driad-Lebeau, and G. Bonnet, "Local amplification of deep mining induced vibrations part.2: simulation of ground motion in a coal basin," *Soil Dynamics and Earthquake Engineering*, vol. 30, no. 10, pp. 947–957, 2010.

[9] W. L. Shen, M. Wang, Z. Z. Cao, F. Q. Su, H. Nan, and X. L. Li, "Mining-induced failure criteria of interactional hard roof structures: a case study," *Energies*, vol. 12, no. 15, 2019.

[10] E. Jiránková, V. Petroš, and J. Šancer, "The assessment of stress in an exploited rock mass based on the disturbance of the rigid overlying strata," *International Journal of Rock Mechanics and Mining Sciences*, vol. 50, pp. 77–82, 2012.

[11] L. Jiang, Q. Wu, Q. Wu et al., "Fracture failure analysis of hard and thick key layer and its dynamic response characteristics," *Engineering Failure Analysis*, vol. 98, pp. 118–130, 2019.

[12] X. B. Li and D. S. Gu, *Rock Impact Dynamics*, Central South University of Technology Press, Changsha, China, 1994.

[13] W. Lei, X. B. Li, A. Taheri, and Q. H. Wu, "Fracture evolution around a cavity in brittle rock under uniaxial compression and coupled static–dynamic loads," *Rock Mechanics and Rock Engineering*, vol. 51, no. 2, pp. 531–545, 2018.

[14] X. Li, F. Gong, M. Tao et al., "Failure mechanism and coupled static-dynamic loading theory in deep hard rock mining: a review," *Journal of Rock Mechanics and Geotechnical Engineering*, vol. 9, no. 4, pp. 767–782, 2017.

[15] D. D. Qin, X. F. Wang, D. S. Zhang, and X. Y. Chen, "Study on surrounding rock-bearing structure and associated control mechanism of deep soft rock roadway under dynamic pressure," *Sustainability-Basel,* vol. 11, no. 7, 2019.

[16] W.-l. Shen, J.-b. Bai, X.-y. Wang, and Y. Yu, "Response and control technology for entry loaded by mining abutment stress of a thick hard roof," *International Journal of Rock Mechanics and Mining Sciences*, vol. 90, no. 12, pp. 26–34, 2016.

[17] Z. W. Li, M. Tao, K. Du, W. Z. Cao, and C. Q. Wu, "Dynamic stress state around shallow-buried cavity under transient P wave loads in different conditions," *Tunnelling and Underground Space Technology*, vol. 97, Article ID 103228, 2020.

[18] M. Patil, D. Choudhury, P. G. Ranjith, and J. Zhao, "Behavior of shallow tunnel in soft soil under seismic conditions," *Tunnelling and Underground Space Technology*, vol. 82, pp. 30–38, 2018.

[19] B. B. Sun, S. R. Zhang, M. J. Deng, and C. Wang, "Nonlinear dynamic analysis and damage evaluation of hydraulic arched tunnels under mainshock-aftershock ground motion sequences," *Tunnelling and Underground Space Technology*, vol. 98, 2020.

[20] Y. Tan, M. S. Yang, and X. Y. Li, "Dynamic response of a circular lined tunnel with an imperfect interface embedded in the unsaturated poroelastic medium under P wave," *Computers and Geotechnics*, vol. 122, Article ID 103514, 2020.

[21] Z. H. Yuan, Z. G. Cao, Y. Q. Cai, X. Y. Geng, and X. Q. Wang, "An analytical solution to investigate the dynamic impact of a moving surface load on a shallowly-buried tunnel," *Soil Dynamics and Earthquake Engineering*, vol. 126, Article ID 105816, 2019.

[22] X. Li, X.-F. Li, Q.-B. Zhang, and J. Zhao, "A numerical study of spalling and related rockburst under dynamic disturbance using a particle-based numerical manifold method (PNMM)," *Tunnelling and Underground Space Technology*, vol. 81, pp. 438–449, 2018.

[23] X. Li, C. Li, W. Cao, and M. Tao, "Dynamic stress concentration and energy evolution of deep-buried tunnels under blasting loads," *International Journal of Rock Mechanics and Mining Sciences*, vol. 104, pp. 131–146, 2018.

[24] X. Li and L. Weng, "Numerical investigation on fracturing behaviors of deep-buried opening under dynamic disturbance," *Tunnelling and Underground Space Technology*, vol. 54, pp. 61–72, 2016.

[25] X. Li, Z. Zhou, T.-S. Lok, L. Hong, and T. Yin, "Innovative testing technique of rock subjected to coupled static and dynamic loads," *International Journal of Rock Mechanics and Mining Sciences*, vol. 45, no. 5, pp. 739–748, 2008.

[26] M. Tao, R. Zhao, K. Du, W. Cao, and Z. Li, "Dynamic stress concentration and failure characteristics around elliptical cavity subjected to impact loading," *International Journal of Solids and Structures*, vol. 191-192, pp. 401–417, 2020.

[27] J. Deng, N. S. Kanwar, M. D. Pandey, and W.-C. Xie, "Dynamic buckling mechanism of pillar rockbursts induced by

stress waves," *Journal of Rock Mechanics and Geotechnical Engineering*, vol. 11, no. 5, pp. 944–953, 2019.

[28] Z. B. Guo, L. Zhang, Z. B. Ma, F. X. Zhong, J. C. Yu, and S. M. Wang, "Numerical investigation of the influence of roof fracturing angle on the stability of gob-side entry subjected to dynamic loading," *Shock and Vibration*, vol. 2019, Article ID 1434135, 13 pages, 2019.

[29] P. Kong, L. S. Jiang, J. Q. Jiang, Y. N. Wu, L. J. Chen, and J. G. Ning, "Numerical analysis of roadway rock-burst hazard under superposed dynamic and static loads," *Energies*, vol. 12, no. 19, 2019.

[30] S.-L. Wang, S.-P. Hao, Y. Chen, J.-B. Bai, X.-Y. Wang, and Y. Xu, "Numerical investigation of coal pillar failure under simultaneous static and dynamic loading," *International Journal of Rock Mechanics and Mining Sciences*, vol. 84, pp. 59–68, 2016.

[31] Z. Y. Wang, L. M. Dou, J. Li, K. Kang, and L. F. Feng, "Numerical investigation of damage risks of roadway surrounding rocks under oblique incident dynamic loads," *Shock and Vibration*, vol. 2017, Article ID 6298372, 13 pages, 2017.

[32] C. J. Hou, *Roadway Surrounding Rock Control*, China University of Mining and Technology Press, Xuzhou, China, 2013.

[33] M. Li, N. Zhou, J. X. Zhang, and Z. C. Liu, "Numerical modelling of mechanical behavior of coal mining hard roofs in different backfill ratios: a case study," *Energies*, vol. 10, no. 7, 2017.

[34] J. Zhang, B. Li, N. Zhou, and Q. Zhang, "Application of solid backfilling to reduce hard-roof caving and longwall coal face burst potential," *International Journal of Rock Mechanics and Mining Sciences*, vol. 88, pp. 197–205, 2016.

[35] Z. Z. Cao, P. Xu, Z. H. Li, M. X. Zhang, Y. Zhao, and W. L. Shen, "Joint bearing mechanism of coal pillar and backfilling body in roadway backfilling mining technology," *CMC-computers Materials & Continua*, vol. 54, no. 2, pp. 137–159, 2018.

[36] H. He, L. Dou, J. Fan, T. Du, and X. Sun, "Deep-hole directional fracturing of thick hard roof for rockburst prevention," *Tunnelling and Underground Space Technology*, vol. 32, pp. 34–43, 2012.

[37] B. Huang, J. Liu, and Q. Zhang, "The reasonable breaking location of overhanging hard roof for directional hydraulic fracturing to control strong strata behaviors of gob-side entry," *International Journal of Rock Mechanics and Mining Sciences*, vol. 103, pp. 1–11, 2018.

[38] W. Wang, Y.-P. Cheng, H.-F. Wang et al., "Fracture failure analysis of hard-thick sandstone roof and its controlling effect on gas emission in underground ultra-thick coal extraction," *Engineering Failure Analysis*, vol. 54, pp. 150–162, 2015.

[39] Y. J. Wang, M. C. He, J. Yang et al., "Case study on pressure-relief mining technology without advance tunneling and coal pillars in longwall mining," *Tunnelling and Underground Space Technology*, vol. 97, 2020.

[40] B. Yu, C. Liu, J. Yang, and J. Liu, "Research on the fracture instability and its control technique of hard and thick roof," *Journal of China University of Mining and Technology*, vol. 42, pp. 342–348, 2012.

[41] S. Liu, X. Li, and D. Wang, "Experimental study on temperature response of different ranks of coal to liquid nitrogen soaking," *Natural Resources Research*, 2020.

[42] R. M. Khafizov, I. G. Khusainov, and V. S. Shagapov, "Dynamics of the pressure relaxation in a "depressurized" borehole," *Journal of Applied Mathematics and Mechanics*, vol. 73, no. 4, pp. 443–448, 2009.

[43] V. S. Shagapov, I. G. Khusainov, and R. M. Khafizov, "Pressure Relaxation in a hole surrounded by porous and

permeable rock in hole pressure tests with gas injection," *Journal of Applied Mechanics and Technical Physics*, vol. 47, no. 1, pp. 91–98, 2006.

[44] V. S. Shagapov, G. Y. Khusainova, I. G. Khusainov, and R. N. Khafizov, "Pressure Relaxation in a hole surrounded by a porous and permeable rock," *Combustion, Explosion, and Shock Waves*, vol. 38, no. 3, pp. 346–351, 2002.

[45] M. Wang, D. Zheng, W. Shen, X. Wang, and W. Li, "Depressurizing boreholes for mitigating large deformation of the main entry," *Energy Science & Engineering*, vol. 8, no. 4, pp. 1404–1417, 2020.

[46] L. Jiang, P. Zhang, L. Chen et al., "Numerical approach for goaf-side entry layout and yield pillar design in fractured ground conditions," *Rock Mechanics and Rock Engineering*, vol. 50, no. 11, pp. 3049–3071, 2017.

[47] W. Li, J. Bai, S. Peng, X. Wang, and Y. Xu, "Numerical modeling for yield pillar design: a case study," *Rock Mechanics and Rock Engineering*, vol. 48, no. 1, pp. 305–318, 2015.

[48] S. Yan, J. Bai, X. Wang, and L. Huo, "An innovative approach for gateroad layout in highly gassy longwall top coal caving," *International Journal of Rock Mechanics and Mining Sciences*, vol. 59, pp. 33–41, 2013.

[49] A. H. Wilson and D. P. Ashwin, "Research into the determination of pillar size," *Minerals Engineering*, vol. 131, no. 141, pp. 409–417, 1972.

[50] C. J. Hou and N. J. Ma, "Stress in in-seam roadway sides and limit equilibrium zone," *Journal of China Coal Society*, vol. 4, pp. 21–29, 1989.

[51] X. Wang, J. Bai, R. Wang, and W. Sheng, "Bearing characteristics of coal pillars based on modified limit equilibrium theory," *International Journal of Mining Science and Technology*, vol. 25, no. 6, pp. 943–947, 2015.

[52] Y. Yu, "Dynamic characteristic of hard roof fracture in extra-thick coal seam and its application on the control of roadway surrounding rock," Ph. D.thesis, China University of Mining and Technology, Xuzhou, China, 2015.

[53] J.-B. Bai, W.-L. Shen, G.-L. Guo, X.-Y. Wang, and Y. Yu, "Roof deformation, failure characteristics, and preventive techniques of gob-side entry driving heading adjacent to the advancing working face," *Rock Mechanics and Rock Engineering*, vol. 48, no. 6, pp. 2447–2458, 2015.

[54] J. F. Labuz and A. Zang, "Mohr-coulomb failure criterion," *Rock Mechanics and Rock Engineering*, vol. 45, no. 6, pp. 975–979, 2012.

[55] F. D. Itasca, *Fast Lagrangian Analysis of Continua in 3 Dimensions, Version 5.0*, Itasca Consulting Group, Minneapolis, MN, USA, 2012.

[56] A. Preh and M. Zapletal, "The perfect mesh for FLAC3D to analyze the stability of rock slopes," in *Proceedings of the 4th International Flac Symposium on Numerical Modeling in Geomechanics*, pp. 1–5, Itasca Consulting Group Inc, Minneapolis, MN, USA, May 2006.

[57] H. P. Kang, J. Lin, L. X. Yan, X. Zhang, Y. Z. Wu, and L. P. Si, "Study on characteristics of underground in-situ stress distribution in Shanxi coal mining fields," *The Chinese Journal of Geophysics-Ch*, vol. 52, no. 7, pp. 1782–1792, 2009.

[58] E. Esterhuizen and M. M. Murphy, "Numerical model calibration for simulating coal pillars, gob and overburden response," in *Proceedings of the Twenty-Ninth International Conference on Ground Control in Mining*, pp. 46–57, Morgantown, WV, USA, July 2010.

[59] W. L. Shen, J. B. Bai, Z. Y. Zhao, X. H. Shen, X. Y. Wang, and J. Z. Kang, "Three indexes method for roadway layout below

the closed residual bearing coal pillar," *Journal of Mining & Safety Engineering*, vol. 35, no. 3, pp. 465–472, 2018.

[60] S. Yang, J. Wang, X. H. Li, J. G. Ning, and P. Q. Qiu, "In situ investigations into mining-induced hard main roof fracture in longwall mining: a case study," *Engineering Failure Analysis*, vol. 106, Article ID 104188, 2019.

[61] H. W. Liu, *Mechanics of Materials (II)*, Higher Education Press, Beijing, China, 4th edition, 2004.

[62] J. Li and G. Ma, "Analysis of blast wave interaction with a rock joint," *Rock Mechanics and Rock Engineering*, vol. 43, no. 6, pp. 777–787, 2010.

[63] M. G. Qian, P. W. Shi, and J. L. Xu, *Mining Pressure and Strata Control*, China University of Mining and Technology Press, Xuzhou, China, 2st edition, 2010.

[64] W. D. Wu, J. B. Bai, X. Y. Wang, S. Yan, and S. X. Wu, "Numerical study of failure mechanisms and control techniques for a gob-side yield pillar in the Sijiazhuang coal mine, China," *Rock Mechanics and Rock Engineering*, vol. 52, no. 6, pp. 1231–1245, 2018.

[65] Q. L. Yao, J. Zhou, Y. N. Li, Y. M. Tan, and Z. G. Jiang, "Distribution of side abutment stress in roadway subjected to dynamic pressure and its engineering application," *Shock and Vibration*, vol. 2015, Article ID 929836, 11 pages, 2015.